Tracing nuclear-wave-packet dynamics in singly and doubly charged states of N_2 and O_2 with XUV-pump–XUV-probe experiments

M. Magrakvelidze,[1] O. Herrwerth,[2] Y. H. Jiang,[3] A. Rudenko,[1,4,5] M. Kurka,[5] L. Foucar,[4] K. U. Kühnel,[5] M. Kübel,[2] Nora G. Johnson,[1,2] C. D. Schröter,[5] S. Düsterer,[6] R. Treusch,[6] M. Lezius,[2] I. Ben-Itzhak,[1] R. Moshammer,[5] J. Ullrich,[4,5,7] M. F. Kling,[1,2,*] and U. Thumm[1,†]

[1] *J.R. Macdonald Laboratory, Department of Physics, Kansas State University, Manhattan, Kansas 66506, USA*

[2] *Max-Planck-Institut für Quantenoptik, 85748 Garching, Germany*

[3] *Shanghai Advanced Research Institute, Chinese Academy of Sciences, Shanghai 201210, China*

[4] *Max-Planck Advanced Study Group at CFEL, 22607 Hamburg, Germany*

[5] *Max-Planck-Institut für Kernphysik, 69117 Heidelberg, Germany*

[6] *DESY, 22607 Hamburg, Germany*

[7] *Physikalisch-Technische Bundesanstalt, D-38116 Braunschweig, Germany*

(Received 8 March 2012; published 18 July 2012)

We traced the femtosecond nuclear-wave-packet dynamics in ionic states of oxygen and nitrogen diatomic molecules employing 38-eV XUV-pump–XUV-probe experiments at the free-electron laser in Hamburg (FLASH). The nuclear dynamics is monitored via the detection of coincident ionic fragments using a reaction microscope and a split-mirror setup to generate the pump and probe pulses. By comparing measured kinetic-energy-release spectra with classical and quantum-mechanical simulations, we identified electronic states of the molecular ions that are populated by ionization of the neutral molecule. For specific fragment charge states, this comparison allows us to assess the relevance of specific dissociation paths.

DOI: 10.1103/PhysRevA.86.013415 PACS number(s): 33.20.Xx, 31.50.−x, 33.80.−b

I. INTRODUCTION

Time-resolved experiments interrogating nuclear-wave-packet dynamics of diatomic and more complex molecules in various charge states offer the possibility to test calculated potential energy surfaces for these species and gain detailed insight into reaction pathways as a function of the excitation conditions [1–4].

So far, the ultrafast nuclear-wave-packet dynamics in various charge states of diatomic molecules were nearly exclusively examined with time-resolved pump-probe spectroscopy using intense few-cycle near-infrared (NIR) laser pulses [1,2,5,6]. However, these pulses with high peak intensities tend to induce strong couplings between dipole-allowed adiabatic molecular states. Accordingly, NIR-pump–NIR-probe spectroscopy very sensitively probes the nuclear dynamics near curve crossings which result from such couplings. Importantly, the localization of NIR-induced couplings at avoided crossings means that NIR-pump–NIR-probe experiments examine the nuclear dynamics of field-dressed rather than external-field-free adiabatic molecular potential curves. Moreover, the presence of intense NIR pulses, in general, perturbs the target of interest significantly, such that those pulses also alter the outcome of chemical reactions. For this reason, strictly speaking, NIR pulses are not suitable for detecting and exploring the nuclear motion on unperturbed potential curves.

Intense, ultrashort extreme ultraviolet (XUV) radiation, on the other hand, are much better suited for this task as detailed below. Recent progress in the development of tunable intense XUV laser sources led to the realization of isolated XUV pulses with pulse durations below 100 as [7]. XUV and x-ray laser pulses are produced by either employing high-harmonic generation [8,9] or free-electron lasers [10]. In contrast to intense NIR pulses, their interaction with atomic and molecular targets is characterized by large Keldysh parameters, corresponding to ionization by the absorption of no more than a few energetic photons. In addition, with regard to identifying reaction pathways, the absorption of a known small number of energetic photons (rather than a large, not-well-determined number of less-energetic photons provided by a NIR pulse of comparable spectral width) tends to induce electronic transitions to a more narrowly defined part of the target electronic spectrum. In addition, since these XUV and x-ray sources are tunable, transitions into specific spectral regions can be selected. In dissociative reactions, the kinetic energy release (KER) can thus be resolved with regard to the number of absorbed photons and the pump-pulse-generated intermediate charge states of the molecular ion. This is done for a comparatively narrow spectral range of intermediate adiabatic states which are populated by short-wavelength pump and probe pulses, facilitating the assignment of possible dissociation (reaction) pathways. Time resolutions on the order of a few femtoseconds can be realized, which is short enough to trace even the fastest motion of nuclei in molecules. Attempts to achieve even higher resolution in time, in order to simultaneously follow the electronic motion during chemical reactions or to zoom into fast rearrangement processes, would decrease the spectral resolution.

Recently, the nuclear-wave-packet dynamics in diatomic molecular ions was investigated in several XUV-pump–NIR-probe experiments [11–16]. Here, the pump pulse is perturbative but the NIR-probe pulse efficiently couples potential energy curves of the molecular ion, making these studies sensitive mainly to confined regions of internuclear distances where

*matthias.kling@mpq.mpg.de
†thumm@phys.ksu.edu

the coupling is strong. XUV-pump–XUV-probe spectroscopy pioneered in [17] removes this limitation. Here, the first XUV pulse ionizes the neutral molecule and initializes a nuclear wave packet in the ionic species of interest and on potential energy curves that lie within a specific spectral range of the molecular ion. The second XUV pulse probes the dynamics by a subsequent ionization step, removing one or several electrons. In contrast to NIR-probe pulses, for sufficiently high XUV photon energy, the final charge state of the molecular ion will be reached for any given pump-probe delay. Hence, the wave-packet motion can be observed along the entire reaction coordinate. In addition, this scheme often leads to multiple ionizations and, as a result, to fragmentation by Coulomb explosion (CE). Measurement of the resulting KER and momentum distributions as a function of the pump-probe delay then enables the imaging of the wave-packet dynamics (if the reflection principles can be applied and the fragmentation potential energy surfaces are known) in the same way as it is done in NIR-pump–NIR-probe CE experiments (see, e.g., [6]), but without the limitations described above. Following this approach, XUV-pump–XUV-probe experiments have recently been conducted to trace the nuclear-wave-packet motion in the D_2 cation [18] and to measure the isomerization dynamics in the acetylene cation [19].

In this publication, we report on XUV-pump–XUV-probe studies performed at FLASH with the goal to elucidate the nuclear-wave-packet dynamics following the XUV ionization of O_2 and N_2 at central photon energies of 38 eV. By comparing our experimental results with classical and quantum-mechanical calculations, based on available potential energy curves for various charge states of these molecules, we describe a method for identifying the dominant dissociation pathways. We use atomic units (a.u.) throughout this work unless indicated otherwise.

II. EXPERIMENTAL METHOD

The three-dimensional momentum vectors of fragment ions were recorded at beamline BL3 of FLASH with a reaction microscope (REMI) [20] equipped with an on-axis back-reflection split-mirror arrangement for focusing and creating a pulse pair (for details see [17,19]). The multilayer XUV mirror had a reflectivity of 30% at 38 eV with a FWHM of 3 eV, suppressing higher harmonics of the free electron laser (FEL) radiation by at least 1 order of magnitude. The temporal overlap between the two XUV pulses was determined by detecting the delay-dependent dissociation of the coincident $O^+ + O^{2+}$ ($N^+ + N^{2+}$) fragments, where a maximum in the dissociation yield at zero delay time was observed [21]. The intensity of the incoming FEL beam was equally distributed over both half mirrors, and the foci were merged inside a dilute and well-localized (less than 1 mm diameter) cold molecular beam in the center of the REMI. With a focus diameter of $\sim$20 μm and pulse energies of a few microjoules at an estimated average pulse duration of $\sim$80 fs [22], we reached peak intensities of the order of 10^{13} W/cm^2 at a photon energy of 38 $\pm$ 0.5 eV. Ionic fragments were projected by means of an electric field (40 V/cm) onto a time- and position-sensitive microchannel plate detector (diameter 120 mm, position resolution 0.1 mm, multihit delay-line readout) and recorded as a function of the pump-probe time delay. From the measured time-of-flight (TOF) and position of each individual fragment, the initial three-dimensional momentum vector was reconstructed. The resolution in the KER is better than 50 meV for all fragment energies detected.

III. THEORETICAL MODELS

In order to identify dissociation pathways in terms of adiabatic electronic states involved in the molecular fragmentation dynamics, we use two separate methods. We first understand the main features in the measured spectra by calculating the KER $K(\tau)$ as a function of the pump-probe delay τ classically [1] by solving Newton's equations for the nuclear motion on adiabatic molecular potential curves. Next, in an alternative and more accurate quantum-mechanical model, we solve the time-dependent Schrödinger equation for the motion of the nuclear wave packet on selected molecular potential curves. This allows us to simulate KER spectra for given dissociation paths, i.e., for a given sequence of adiabatic molecular states that are successively populated by ionization of the neutral molecule with the pump and, subsequently, of the molecular ion with the probe XUV pulse. Finally, by comparing the simulated and measured KER spectra, we attempt to assess the importance of specific dissociation pathways considered in our quantum calculations.

A. "Classical" simulations

In this model the XUV pump pulse is assumed to instantaneously ionize the neutral molecule by removing one or more electrons at time zero. In response, the nuclei are assumed to start moving as classical point particles on a selected intermediate (bonding) adiabatic molecular potential curve of the molecular ion in a specific charge state and at an internuclear distance R that is equal to the equilibrium distance in the neutral molecule before ionization. This modeling of the pump process corresponds to the Franck-Condon (FC) approximation in quantum-mechanical calculations. The subsequent nuclear motion is described by solving Newton's equations of motion for the selected adiabatic potential curve of the molecular ion.

Similarly, the delayed XUV probe pulse is assumed to instantaneously (multiply) ionize the molecular ion at the pump-probe delay time τ. The nuclei start their classical motion after the probe pulse with the relative velocity they had just before the action of the probe pulse. Their classical motion after the probe pulse is assumed to be dissociative and to proceed on a repulsive Coulomb potential curve α/R, with $\alpha = qp$, where q and p are the charges of the two fragments. The KER for a given delay is thus obtained by adding the kinetic energy of the relative motion of the nuclei at time τ and to the Coulomb repulsion energy $\alpha/R(\tau)$ (see [1,2] for details). This calculation is repeated for several intermediate adiabatic electronic states.

B. Quantum-mechanical simulations

As for our classical model, we describe the action of both the XUV pump and XUV probe pulses as a sudden removal of one or more electrons. Prior to the pump pulse, for times

$t < 0$, we assume the neutral molecule to be in its electronic and vibrational ground state. The instantaneous ionization of the neutral molecule by the pump pulse is modeled to result in a vertical (FC) transition to a preselected bonding adiabatic potential curve $E_i(R)$ of the molecular ion in a given charge state, on which a nuclear vibrational wave packet $\Psi(R,t)$ starts to evolve. This wave packet can be thought of as a coherent superposition $\Psi(R,t) = \sum_\nu a_\nu \exp(-i\omega_\nu t)\varphi_\nu(R)$ of vibrational eigenstates φ_ν with energies ω_υ in the selected potential curve $E_i(R)$. In the absence of external fields, $\Psi(R,t)$ propagates freely on $E_i(R)$, starting at time $t = 0$ as the vibrational ground state of the *neutral* parent molecule. We obtain $\Psi(R,t)$ by propagating the time-dependent Schrödinger equation for 300 fs with time steps of $\Delta t = 1$ atomic unit (a.u.) on a numerical grid that covers the interval $0 \leqslant R \leqslant 100$ a.u. with equidistant grid spacing $\Delta R = 0.02$ a.u. [23].

The free propagation of $\Psi(R,t)$ on $E_i(R)$ is interrupted by the probe pulse at the delay time τ. This action further ionizes the molecular ion and is assumed to instantaneously project the nuclear wave function onto a dissociative final adiabatic molecular potential curve $E_f(R)$. We thus obtain the KER distribution,

$$Y(K,\tau) = |\Psi(R(K),\tau)|^2 \left|\frac{dE_f(R)}{dR}\right|^{-1}, \quad (1)$$

by mapping the nuclear probability density $|\Psi(R,\tau)|^2$ at a given delay onto $E_f(R)$. For dissociation along a pure Coulomb potential curve $E_f(R) = \alpha/R$, Eq. (1) simplifies to

$$Y(K,\tau) = |\Psi(R(K),\tau)|^2 \frac{R^2}{\alpha}. \quad (2)$$

Note that K in Eqs. (1) and (2) is the sum of the kinetic energies released by the two nuclei. Note also that these transformations neglect the kinetic energy, $E_{\rm kin} = \langle\Psi(R,t)|\hat{K}|\Psi(R,t)\rangle$, of the nuclei at the ionization time $t = \tau$ [23], where $\hat{K}$ is the operator for the relative kinetic energy of the nuclei. We include $E_{\rm kin}$ in our quantum-mechanical simulation by shifting the argument in the right-hand sides of Eqs. (1) and (2) according to

$$Y(K_{\rm tot},\tau) = |\Psi(R(K_{\rm tot} - E_{\rm kin}),\tau)|^2 \left|\frac{dE_f(R)}{dR}\right|^{-1}, \quad (3)$$

where $K_{\rm tot} = K + E_{\rm kin}$ and the R derivative is taken without including $E_{\rm kin}$, i.e., at $R(K_{\rm tot} - E_{\rm kin})$. In our numerical calculations below, we find small contributions of $E_{\rm kin}$ that do not exceed 0.5 eV for the oxygen and 0.3 eV for the nitrogen targets. The inclusion of $E_{\rm kin}$ does not noticeably affect the comparison with measured KER spectra discussed in the following sections.

IV. RESULTS AND DISCUSSION

A. Oxygen

The relevant lowest potential curves for O_2, O_2^+, and O_2^{2+} molecules, adapted from [24–26], are given in Fig. 1. States with gerade symmetry are plotted in Fig. 1(a) as dashed lines (including the ground states of the O_2 and O_2^+ molecules) and ungerade states are given as solid lines. Similarly, states with gerade (dashed lines) and ungerade (solid lines) symmetry are shown in Fig. 1(b) for O_2^{2+}. The pure $1/R$ Coulomb potential, shifted to match the dissociation limit at 39.0 eV, is shown as a dotted line in Fig. 1(b).

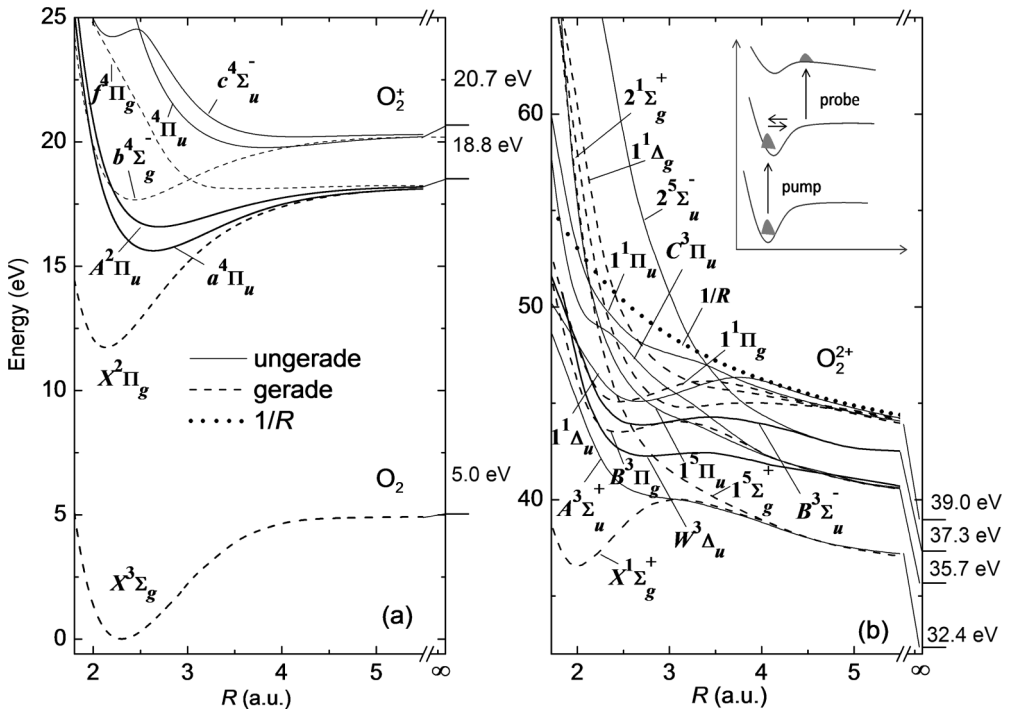

FIG. 1. Adiabatic electronic states for (a) neutral O_2 and the O_2^+, and (b) the O_2^{2+} molecular ion adapted from [26,31,32]. Gerade states are indicated as dashed lines and ungerade states as solid lines. The repulsive $1/R$ Coulomb potential, shifted to match the 39.0 eV dissociation limit, is shown as a dotted line. Dissociation limits are indicated to the right of the potential curves.

Figure 2 shows the measured KER vs pump-probe delay for the $O_2 \rightarrow O^+ + O^+$ (a), $O_2 \rightarrow O^{2+} + O^+$ (b), $O_2 \rightarrow O^{2+} + O^{2+}$ (c) dissociation channels (on the right) alongside the delay-integrated KER spectra (on the left). The breakup channels can be reached by various pathways. An analysis of the intensity-dependent yield (as done in Ref. [22] for N_2^{q+}) indicates that the $O_2 \rightarrow O^+ + O^+$ channel involves two photons, the $O_2 \rightarrow O^{2+} + O^+$ channel three photons, and the $O_2 \rightarrow O^{2+} + O^{2+}$ channel between four and six photons. Note that energy conservation alone merely requests the absorption of one (two) photon(s) to generate singly (doubly) charged molecular ions. At the intensities used in the current study, the $O_2 \rightarrow O^+ + O^+$ channel can be populated both directly and sequentially, where the latter involves intermediate O_2^+ states. The distinct peaks in Fig. 2(a), labeled a–d, can be assigned to the direct population of the O_2^{2+} $W\ ^3\Delta_u, B\ ^3\Sigma_u^-$, $1\ ^1\Delta_u$, and $B\ ^3\Pi_g$ states [24,27].

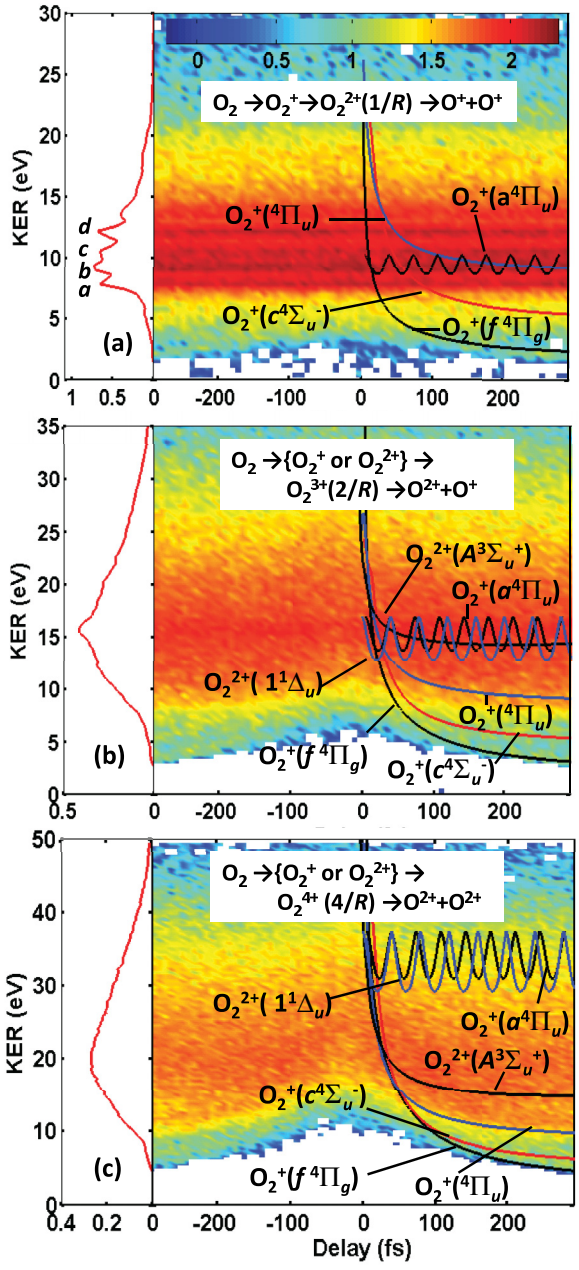

FIG. 2. (Color online) Measured KER spectra as a function of the pump-probe delay τ (same logarithmic color/gray scale for the fragment yield in all plots) compared with the classically calculated KER curves $K(\tau)$ for different breakup channels: (a) $O^+ + O^+$, (b) $O^{2+} + O^+$, and (c) $O^{2+} + O^{2+}$. The delay-integrated KER spectra are shown on the left. The classical calculations were done using the dissociative $f\ ^4\Pi_g$, $c\ ^4\Sigma_u\ ^-$,$^4\Pi_u$, and bound $a\ ^4\Pi_u$ states of O_2^+ and the dissociative $A\ ^3\Sigma_u^+$ and the bound $1\ ^1\Delta_u$ states of O_2^{2+}.

In Fig. 2 we compare the experimental data to the classically calculated KER lines for the intermediate electronic states $f\ ^4\Pi_g$, $c\ ^4\Sigma_u^-$, $^4\Pi_u$,$a\ ^4\Pi_u$ of the O_2^+ molecule, and $A\ ^3\Sigma_u^+$, $1\ ^1\Delta_u$ of the O_2^{2+} molecule (the latter being relevant for the sequential population of triply and quadruply charged O_2). Note that the angular distributions of the fragment emission can in principle help to narrow down the choices for intermediate states. For the measurement on O_2, however, the limited signal-to-noise ratio did not allow exclusion of any intermediate states based on the fragment angular distributions. For our calculations in Fig. 2, we assumed dissociation along the α/R Coulomb potentials with potential strengths $\alpha = qp$ in the breakup channels $O_2 \rightarrow O^{q+} + O^{p+}$. The KER lines are strikingly different for dissociation paths that involve dissociative and bonding intermediate states. While dissociative intermediate states ($f\ ^4\Pi_g$, $c\ ^4\Sigma_u^-$, $^4\Pi_u$,$A\ ^3\Sigma_u^+$) yield KER lines which decrease monotonously as functions of the pump-probe delay, the bound and predissociating intermediate states, $a\ ^4\Pi_u$, $1\ ^1\Delta_u$, yield KER lines that oscillate with periods of 34 and 41 fs, respectively. For the bound and predissociating intermediate states, the calculated asymptotic energies are in good agreement with the measured spectra, except for the $O_2 \rightarrow O^{2+} + O^{2+}$ dissociation channel. Performing separate classical calculations using all bound states in Fig. 1 as intermediate states, we found that none could reproduce the dissociative energy limit measured for the $O_2 \rightarrow O^{2+} + O^{2+}$ channel.

Next we carried out quantum-mechanical calculations, including those intermediate states which best reproduced the measured KER limits in our classical calculations in Figs. 2(a) and 2(b), with exception of the $O_2 \rightarrow O^{2+} + O^{2+}$ channel. Since, for this particular channel, dissociation through bound intermediate states does not reproduce the measured data, we also performed a separate calculation including the dissociative $A\ ^3\Sigma_u^+$ state of O_2^{2+}, which yields the best agreement with the measured KER spectrum in Fig. 2(c). Figure 3 shows a comparison between the measured KER values for positive delays (left column) and the results from our quantum-mechanical calculations (middle and right column) for the dissociation channels: $O_2 \rightarrow O^+ + O^+$ (top), $O_2 \rightarrow O^{2+} + O^+$ (middle), and $O_2 \rightarrow O^{2+} + O^{2+}$ (bottom row). In the calculations for the $O^+ + O^+$ dissociation channel, the XUV pump pulse singly ionizes O_2 and the XUV probe pulse removes a second electron, moving the nuclear wave packet onto O_2^{2+} states and causing dissociation. Explicitly, the wave packet is launched from the O_2 ground state via a FC transition onto the bound potential curve of the O_2^+ ($a\ ^4\Pi_u$) state.

We also calculated KER spectra for dissociation along the $2\ ^1\Sigma_g^+$, $1\ ^1\Delta_g$, $1\ ^1\Pi_g$, and $B\ ^3\Pi_g$ repulsive states of O_2^{2+} (not shown) and obtained KER spectra that agree

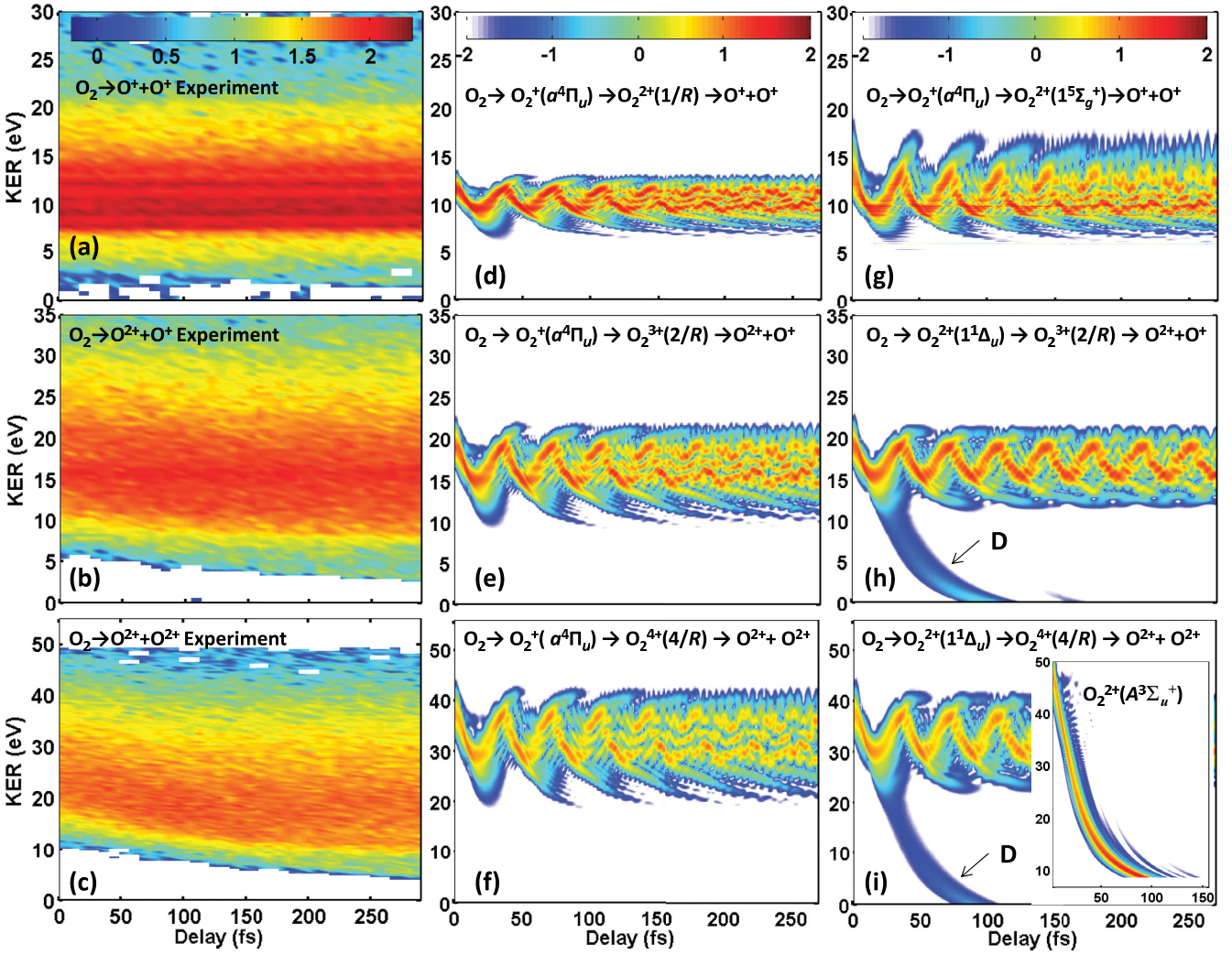

FIG. 3. (Color online) (a) Measured KER spectra as a function of pump-probe delay τ for the $O_2 \rightarrow O^+ + O^+$ breakup channel and (d, g) corresponding quantum-mechanical calculations. (b) Measured KER spectra for the $O_2 \rightarrow O^{2+} + O^+$ channel and (e, h) corresponding quantum-mechanical calculations. (c) Measured KER spectra for the $O_2 \rightarrow O^{2+} + O^{2+}$ breakup channel and (f, i) corresponding quantum-mechanical calculations (same logarithmic color/gray scales for the fragment yield within each column). The dissociation bands are marked "D" (see text). The measured KER spectra are taken from Fig. 2 for positive delays and shown on a slightly different color/gray scale, as indicated. The inset in panel (i) shows the calculated KER for the dissociative intermediate state $O_2^{2+}(A\ ^3\Sigma_u^+)$.

equally well with the experimental results in Figs. 3(a)–3(c). Figure 3(d) shows the result for the intermediate bound O_2^+ ($a\ ^4\Pi_u$) state that is Coulomb imaged onto a final $1/R$ state, while the same intermediate state imaged onto the $1\ ^5\Sigma_g^+$ state of O_2^{2+} is considered in Fig. 3(g). For both cases, the position of the energy bands in the KER is in agreement with the measurement. This indicates that populating the O_2^+ ($a\ ^4\Pi_u$) intermediate state is consistent with the measured dissociation dynamics in the $O^+ + O^+$ breakup channel. We found equally good agreement with the experimental data, with a slightly larger oscillation period, by replacing the O_2^+ ($a\ ^4\Pi_u$) intermediate state with the O_2^+ ($A\ ^2\Pi_u$) state (not shown). Similarly, by substituting the O_2^+ ($a\ ^4\Pi_u$) intermediate state with either the O_2^+ ($X\ ^2\Pi_g$) or O_2^+ ($b\ ^4\Sigma_g^-$) state, we obtained spectra (not shown) with a smaller oscillation period than the calculated spectra in Figs. 3(d) and 3(g) that, however, agree equally well with the experimental data in Fig. 3(a). The unambiguous identification of one (or several) intermediate states would require experiments with shorter XUV pulses that are able to resolve the vibrational motion in the molecular ions. The larger spread in KER for dissociation on the O_2^{2+} ($1\ ^5\Sigma_g^+$) potential curve [Fig. 3(g)] relative to the Coulomb explosion in Fig. 3(d) is consistent with the steeper decrease with R of the $1\ ^5\Sigma_g^+$ curve compared with the $1/R$ Coulomb curve [cf., Fig. 1(b)] in the FC region near the equilibrium position of the O_2^+ ($a\ ^4\Pi_u$) curve.

For the dissociation channels $O_2 \rightarrow O^{2+} + O^+$ and $O_2 \rightarrow O^{2+} + O^{2+}$, the KER spectra are calculated assuming a probe-pulse-induced Coulombic explosion along the $2/R$ and $4/R$ curves [Figs. 3(e), 3(h), 3(f), and 3(i)], respectively, and compared with the experimental data for positive delays [Figs. 3(b) and 3(c)]. In particular, Fig. 3(e) shows the quantum-mechanically calculated KER for Coulomb explosion out of an intermediate bonding state of the *singly charged* O_2^+ ion

along the dissociation path $O_2 \rightarrow O_2^+(a\ ^4\Pi_u) \rightarrow O_2^{3+}(2/R) \rightarrow O^{2+} + O^+$, while in Fig. 3(h) dissociation is modeled for an intermediate adiabatic state of the *doubly charged* O_2^{2+} ion, specifically, $O_2 \rightarrow O_2^{2+}(1\ ^1\Delta_u) \rightarrow O_2^{3+}(2/R) \rightarrow O^{2+} + O^+$. For both dissociation paths, the position of the energy band in the calculated KER agrees with the experimental data. However, the dissociative branch for delays below 120 fs [labeled "D" in Figs. 3(h) and 3(i)] is not seen in the experimental data. This track of decreasing KER corresponds to dissociation of the most energetic vibrational components of the initial wave packet after approximately half a vibrational period ($T_{vib} = 41$ fs) in the O_2^{2+} $(1\ ^1\Delta_u)$ potential curve [cf. Fig. 1(b)]. In our FC model for the pump process, a significant fraction of unbound nuclear states of the O_2^{2+} $(1\ ^1\Delta_u)$ potential are populated, since the equilibrium distance of the O_2 ground state lies well within the repulsive part above the shallow well of the O_2^{2+} $(1\ ^1\Delta_u)$ potential curve [cf. Fig. 1(b)].

For the Coulomb explosion by the probe pulse leading to $O^{2+} + O^{2+}$ fragmentation [Figs. 3(f) and 3(i)], our quantum-mechanical calculations overestimate the measured KER, indicating that fragmentation along a pure Coulomb potential is inappropriate in this case. As for the $O^{2+} + O^+$ breakup in Fig. 3(h), our calculated spectrum in Fig. 3(i) shows the dissociative branch (D) emerging from the intermediate O_2^{2+} $(1\ ^1\Delta_u)$ state, which is not seen in the experimental data. The wave-packet oscillations in our quantum-mechanical calculations in Fig. 3 are not resolved in the experimental data. The periods of these oscillations in the calculated KER are consistent with the oscillation periods we obtain directly from the intermediate-state potential energy curves. By fitting these potential curves to Morse potentials [28], we obtain periods of ∼37 and ∼40 fs, respectively, for the intermediate bound states $O_2^+(a\ ^4\Pi_u)$ and $O_2^{2+}(1\ ^1\Delta_u)$, in good agreement with the oscillations in Figs. 3(d)–3(i). We are confident that Coulomb explosion (along the $4/R$ potential curve) is a realistic assumption and performed simulations with the $2\ ^1\Sigma_g^+$, $1\ ^1\Delta_g$, $1\ ^1\Pi_g$, and $B\ ^3\Pi_g$ repulsive intermediate states of O_2^{2+} (not shown), replacing the $O_2^+(a\ ^4\Pi_u)$ and $O_2^{2+}(1\ ^1\Delta_u)$ states in Figs. 3(f) and 3(i). However, these simulations did not improve the agreement with the measured spectrum in Fig. 3(c). Simulations for the dissociative $O_2^{2+}(A\ ^3\Sigma_u^+)$ state, which gives the closest match to the measured KER in the classical calculations [Fig. 2(c)] are shown in the inset in Fig. 3(i). The calculated KER for this intermediate state follows the classically calculated KER line. For the $O^{2+} + O^{2+}$ breakup, our simulations fail to reproduce the measured overall slow decrease in KER for increasing pump-probe delay.

In view of the limited resolution of the measured spectra, our classical and quantum simulations are in good agreement with the experimental data for the $O_2 \rightarrow O^+ + O^+$ and $O_2 \rightarrow O^+ + O^{2+}$ breakup channels. In contrast, for the $O_2 \rightarrow O^{2+} + O^{2+}$ channel our simulations, both classical and quantum mechanical, predict larger KERs than the experiment, not only for the intermediate states employed to calculate the results shown in Figs. 2(c), 3(f), and 3(i), but also for all other intermediate states of O^+ and O^{2+} (not shown) for which we found adiabatic potential curves in the literature (cf. [24–26]). The lack of agreement for this particular dissociation channel might in part be related to (i) pump-pulse-induced dipole couplings between adiabatic intermediate states of O^+ and O^{2+} and (ii) dissociation along potential curves of O^{4+} that deviate from pure $4/R$ Coulomb curves at smaller internuclear distances. The latter effect has been addressed by Quaglia *et al.* [29] in the intensity-dependent laser-induced dissociation of O^{4+}. Their measured KERs for IR-laser peak intensities between 6×10^{14} and 6×10^{15} W/cm^2 are between 4 and 21 eV smaller than predicted by Coulomb explosion at the ground-state equilibrium distance of neutral O_2. The decrease of the KER due to deviations from pure Coulomb dissociation in their IR experiments is thus comparable to the mismatch we find between our measured and simulated results for the $O^{2+} + O^{2+}$ channel. We addressed both effects (i) and (ii), based on *ab initio* calculations of O_2^+,O_2^{2+}, and O_2^{4+} adiabatic potential curves, allowing for dipole couplings of selected electronic states in the electric fields of the XUV pump and probe pulses in a forthcoming publication [30]. We also intend to scrutinize to what degree the simultaneous (coherent versus incoherent) population of vibrational wave packets in two (or more) electronic states by the pump pulse changes the KER. To start with, we plan to investigate the correlated creation of wave packets onto the $O^{2+}(1\ ^1\Delta_u)$ and $O^+(A\ ^3\Sigma_u^+)$ states in a quantum-mechanical calculation.

B. Nitrogen

Adiabatic electronic potential curves for N_2, N_2^+, and N_2^{2+}, adapted from [31,32], are shown in Fig. 4. States with gerade symmetry are plotted as dashed lines [including the ground states of the N_2 and N_2^+ molecules in Fig. 4(a)] and those with ungerade symmetry as solid lines. Similarly, states with gerade (dashed lines) and ungerade (solid lines) symmetry are shown in Fig. 4(b) for N_2^{2+}. The pure $1/R$ Coulomb curve, shifted to match the dissociation limit at 38.9 eV, is given as a dotted line in Fig. 4(b).

As in Sec. IV A, we assume in our classical simulations that the pump pulse populates a *selected* intermediate state of the molecular ion in a *given* charge state, out of which the probe pulse induces fragmentation. Figure 5 shows the measured KER vs pump-probe delay for the dissociation channels $N^+ + N^+$, $N^{2+} + N^+$, and $N^{2+} + N^{2+}$ alongside the delay-integrated KER spectra. Analysis of the intensity-dependent yields (cf. Ref. [22]) indicates that the number of photons needed to populate these channels is 2, 3, and 4–6, respectively, while energy conservation merely requires one (two) XUV photon(s) to generate singly (doubly) charged molecular ions. These experimental results are compared with classically calculated KER curves that are obtained (i) based on the intermediate electronic state $2\ ^2\Pi_u$, $2\ ^2\Sigma_u$, $3\ ^2\Pi_u$, $3\ ^2\Sigma_g$, $4\ ^2\Pi_u$, $4\ ^2\Sigma_u$, $5\ ^2\Pi_u$, or $B\ ^2\Sigma_u^+$ of N_2^+ or $a\ ^3\Pi_u$, or $D\ ^3\Sigma_u^+$ of N_2^{2+}, and (ii) for $\alpha = 1$, 2, or 4, depending on the breakup channel. Preliminary data for angular distributions measured for the N^+ fragment emission from the dissociation of N_2^{2+} into $N^+ + N^+$ indicate predominantly parallel transitions in the energy windows 0–5 eV, 10–13 eV and perpendicular transitions for 5–10 eV and 13–20 eV. The asymptotic energies and dissociation traces appear to be in agreement with the measured spectra. Similar to the O_2 molecule, the calculations, including bound states $B\ ^2\Sigma_u^+$ of N_2^+ and $D\ ^3\Sigma_u^+$ of N_2^{2+}, show

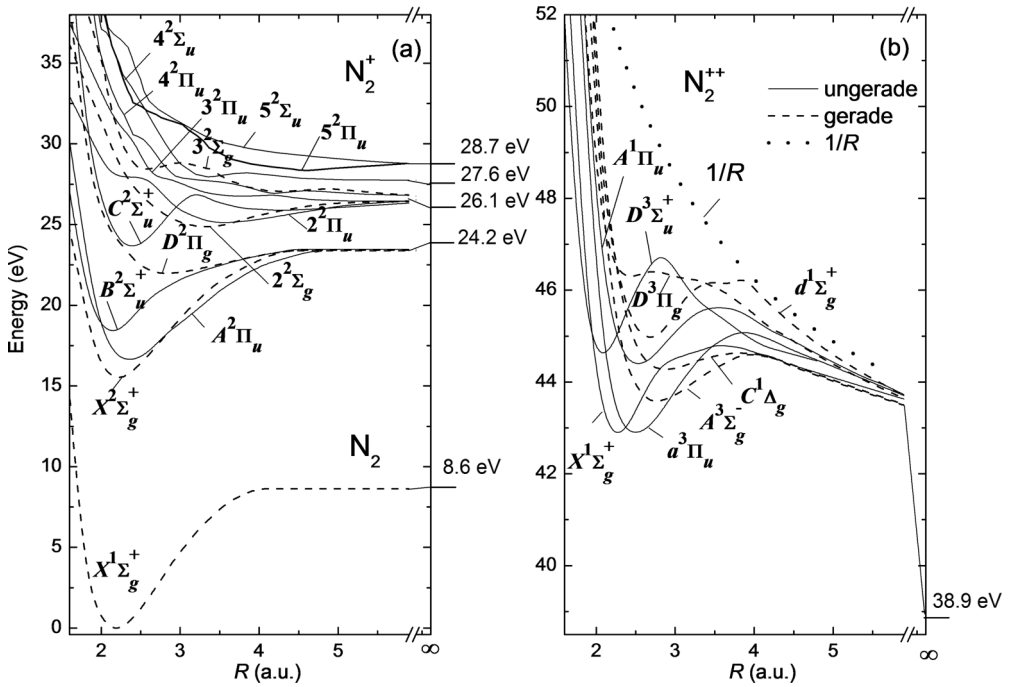

FIG. 4. Adiabatic electronic states for (a) neutral N_2 and the N_2^+, and (b) the N_2^{2+} molecular ion adapted from [26,31,32]. Gerade states are indicated as dashed lines and ungerade states as solid lines. The repulsive $1/R$ Coulomb potential, shifted to match the 38.9 eV dissociation limit, is shown as a dotted line. Dissociation limits are indicated to the right of the potential curves.

oscillations related to the periodic wave-packet motion. Their oscillation period is about 16 fs. All of the bound states we considered in our calculations for the $N^+ + N^+$ dissociation channels [Fig. 4(a)] reproduced KERs of approximately 10 eV. The peaks labeled e and f in Fig. 5(a) are in agreement with a direct population of the N_2^{2+} $A\ ^1\Pi_u$ and $d\ ^1\Sigma_g^+$ states [27,32].

Figures 6(a)–6(c) show the measured KER spectra for positive delays compared to the results from quantum-mechanical calculations (described above) for the dissociation channels $N_2 \rightarrow N^+ + N^+$ (top), $N_2 \rightarrow N^{2+} + N^+$ (middle), and $N_2 \rightarrow N^{2+} + N^{2+}$ (bottom row). Calculations for the $N^+ + N^+$ breakup channel [Figs. 6(d) and 6(g)] were carried out as for the O_2 molecule in Sec. A. Starting from the ground state of N_2, a nuclear wave packet is launched on the N_2^+ ($B\ ^2\Sigma_u^+$) potential curve via a FC transition, and dissociation by the probe pulse is modeled as either Coulomb explosion [Fig. 6(d)] or dissociation in the N_2^{2+} ($D\ ^3\Pi_g$) electronic state [Fig. 6(g)]. For separate calculations with CE-imaged intermediate states $X\ ^2\Sigma_g^+$, $A\ ^2\Pi_u$, or $C\ ^2\Sigma_u^+$ of N_2^+, we obtained KER spectra (not shown) at the same level of (dis)agreement with the experimental data in Fig. 6(a) as our calculated spectra shown in Fig. 6(d). Similarly, if these intermediate states are mapped onto the N_2^{2+} ($D\ ^3\Pi_g$) potential curve, we found similar KER spectra (not shown) that agree equally well with the experimental data in Fig. 6(a) as our calculated spectra in Fig. 6(g). The KER band for $1/R$ Coulomb explosion [Fig. 6(d)] tends to exceed the measured KER, while the calculation is in better agreement with the measurement for dissociation along the N_2^{2+} ($D\ ^3\Pi_g$) potential curve [Fig. 6(g)]. More specifically, the calculated KER for Coulomb explosion in Fig. 6(d) is ∼6 eV larger than for dissociation on the non-Coulombic repulsive N_2^{2+} ($D\ ^3\Pi_g$) state in Fig. 6(g). This is consistent with the potential energy diagrams in Fig. 4, where in the FC region of the N_2^+ ($B\ ^2\Sigma_u^+$) state (roughly between 2 and 2.5 a.u.), the shifted $1/R$ curve is energetically ∼5 eV higher than the $D\ ^3\Pi_g$ state. Note that this discrepancy does not emerge for the O_2 molecule, where the $1/R$ curve happens to be energetically comparable to the O_2^{2+} ($1\ ^5\Sigma_g^+$) state [cf. Fig. 1(b)] in the FC region of the $O_2^+(a\ ^4\Pi_u)$ state.

For $N_2 \rightarrow N^{2+} + N^+$ and $N_2 \rightarrow N^{2+} + N^{2+}$ dissociation the calculated KER plots are shown for Coulomb explosion along $2/R$ and $4/R$ repulsive curves in Figs. 6(e) and 6(h) and Figs. 6(f) and 6(i), respectively, and are compared with the experimental spectra for positive pump-probe delays in Figs. 6(b) and 6(c). For these dissociation processes, the calculated KERs are generally in good agreement with the experimental data. This is in contrast to the O_2 results for the highest-charged dissociation channel $O_2 \rightarrow O^{2+} + O^{2+}$, where the calculated KER spectra do not reproduce the measured data. Nevertheless, our simulated KERs for $N_2 \rightarrow N^{2+} + N^{2+}$ dissociation are clearly larger than the center of energy of the measured KERs [Figs. 6(c), 6(f) and 6(i)]. Even though less pronounced than for the case of $O_2 \rightarrow O^{2+} + O^{2+}$ dissociation, this might in part be due to dissociation along non-Coulombic potential curves of N^{4+} [29]. As for the case of O_2, we plan to address in future simulations non-Coulomb and dipole-coupling effects, and effects that are due to the initial creation by the pump pulse of nuclear vibrational wave packets on more than one adiabatic potential curve. These simulations will include independent *ab initio* calculations of N_2^+, N_2^{2+}, and N_2^{4+} potential curves [30].

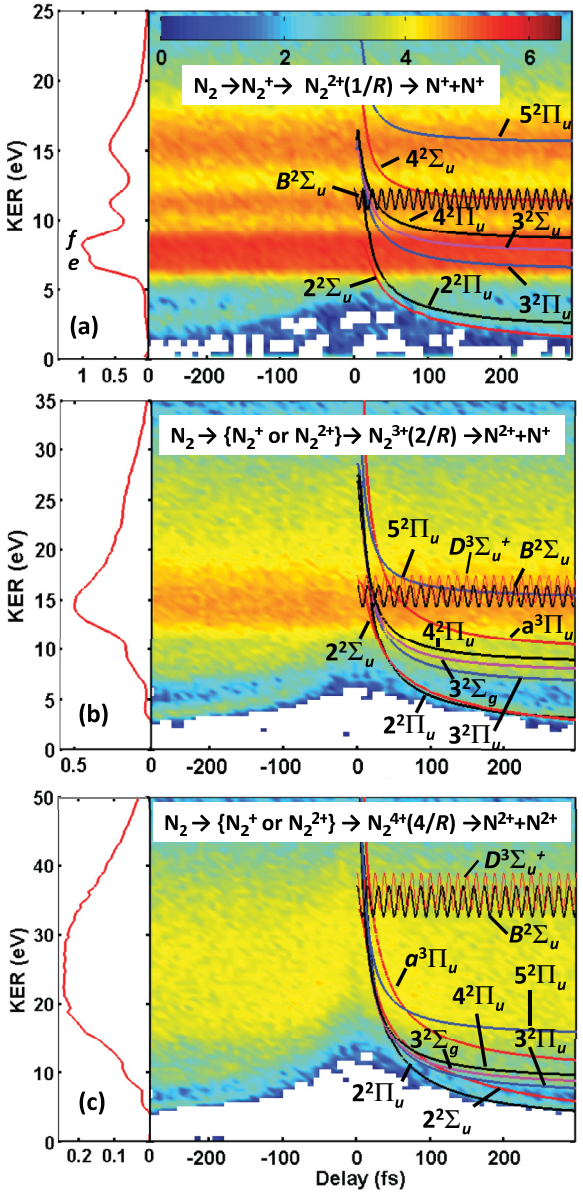

FIG. 5. (Color online) Measured KER spectra as a function of pump-probe delay τ (same logarithmic color/gray scale for the fragment yield in all plots) compared with the classically calculated KER curves $K(\tau)$ for different breakup channels: (a) $N^+ + N^+$, (b) $N^{2+} + N^+$, and (c) $N^{2+} + N^{2+}$. The delay-integrated KER spectra are shown on the left. The classical calculations were done for the dissociative $2\,^2\Sigma_u$, $2\,^2\Pi_u$, $3\,^2\Pi_u$, $3\,^2\Sigma_g$, $4\,^2\Pi_u$, $4\,^2\Sigma_u$, $5\,^2\Pi_u$, and the bound $B\,^2\Sigma_u^+$ states of N_2^+ and the dissociative $a\,^3\Pi_u$ and bound $D\,^3\Sigma_u^+$ states of N_2^{2+}.

In our search for relevant intermediate N_2^+ electronic states, we included all potential curves that are reproduced in Fig. 4(a) [26,31,32]. These electronic states include most of the states identified in the analysis of the N_2^+ vibrational structure with He II radiation in the spectral range between 23 and 35 eV by Baltzer *et al.* [33]. With regard to the few electronic states of N_2^+ discussed by Baltzer *et al.* but not considered by us, potential curves are not available to us. We nevertheless are confident that none of these states would noticeably further improve the agreement we find between our simulated and measured spectra. As for the dissociation of the O_2 molecule, our quantum-mechanical calculations for the dissociation of N_2 in Fig. 6 predict wave-packet oscillations that are not resolved in the experimental data. By fitting the potential curves for the intermediate states N_2^+ ($B\,^2\Sigma_u^+$) and N_2^{2+} ($D\,^3\Sigma_u^+$) to Morse potentials [28], we obtain periods of ~16 and ~15 fs, respectively, in good agreement with the oscillations in Figs. 6(d)–6(i).

V. SUMMARY AND OUTLOOK

Our classical calculations reproduce the main features of the measured KER spectra. This indicates that following the classical nuclear dynamics on quantum-mechanical adiabatic potential curves is a valid scheme for approximating the dissociation dynamics of homonuclear diatomic molecules (with limited accuracy). In comparison with measured KER spectra we find good agreement for the dissociation of oxygen molecules via XUV-pumped transitions to specific intermediate states of O_2^+ or O_2^{2+}. These intermediate states are assumed to fragment upon irradiation with the XUV probe pulse. The same was found for the dissociation of nitrogen molecules.

In our quantum-mechanical simulations, we investigated different dissociation paths by calculating KER spectra separately for different (intermediate and dissociating) adiabatic electronic states of $O_2^{+,2+}$ and $N_2^{+,2+}$ molecular ions. These simulated KER spectra are (for most cases) compatible with the experimental data. For $N^+ + N^+$ dissociative ionization of N_2, our quantum-mechanical calculation predicts different KERs for $1/R$ Coulomb explosion and dissociation along the N_2^{2+} ($D\,^3\Pi_g$) antibonding state. In contrast, for $O^+ + O^+$ dissociation of O_2, we find that Coulomb explosion and dissociation along the O_2^{2+} ($1\,^5\Sigma_g^+$) state yield comparable KERs. Interestingly, for the $N_2 \rightarrow N^{2+} + N^{2+}$ dissociation channel, Coulomb explosion produces KER spectra that agree with the measured data, while this is not the case for the $O_2 \rightarrow O^{2+} + O^{2+}$ dissociation channel [Figs. 3(f) and 3(i)]. Overall, taking the limited resolution of the measured spectra into account, our classical and quantum simulations are in good agreement with the experiments, with the exception of the $O_2 \rightarrow O^{2+} + O^{2+}$ channel. We hope to resolve this lack of agreement in the future by employing quantum-mechanical simulations. These simulations will explore additional simulation paths by including more than one (dipole-coupled) intermediate state [30] and should be based on experimental XUV-pump–XUV-probe data with improved statistics and time resolution, taken for a large range of pump-probe delays, which will allow us to apply additional criteria for the selection of dissociation pathways, such as nuclear oscillation periods and revival times. Another possible reason for the lack of agreement between measured and simulated KER spectra for the $O^{2+} + O^{2+}$ channel might be the ionization of singly-charged fragments at larger internuclear distances. This would be compatible with the relatively long XUV pulses used in the experiments and the kinetic energy being mainly accumulated along a $O^+ + O^{2+}$ potential curve but accounted for in the $O^{2+} + O^{2+}$ channel.

The measured spectra discussed in this work were recorded with XUV pulse lengths that are slightly longer than the

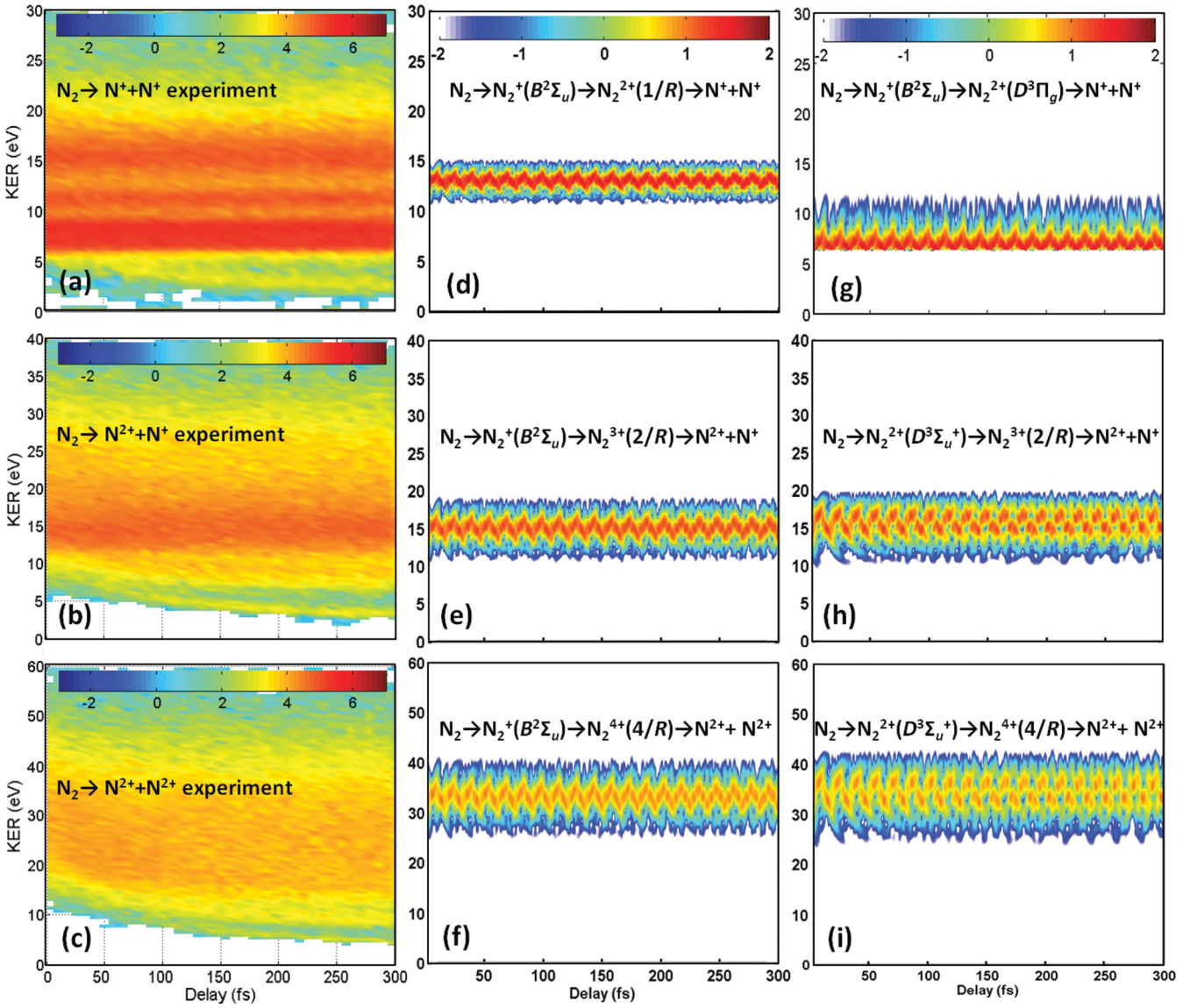

FIG. 6. (Color online) (a) Measured KER spectra as a function of pump-probe delay τ for the $N_2 \rightarrow N^+ + N^+$ breakup channel and (d, g) corresponding quantum-mechanical calculations. (b) Measured KER spectra for the $N_2 \rightarrow N^{2+} + N^+$ channel and (e, h) corresponding quantum-mechanical calculations. (c) Measured KER spectra for the $N_2 \rightarrow N^{2+} + N^{2+}$ breakup channel and (f, i) corresponding quantum-mechanical calculations (same logarithmic color/gray scales for the fragment yield within each column). The measured KER spectra are taken from Fig. 2 for positive delays and shown on a different color/gray scale, as indicated.

nuclear vibrational periods for O_2 and N_2 molecular ions and thus prohibited the unambiguous identification of intermediate states and dissociation paths. Future XUV-pump–XUV-probe experiments with shorter pulses and higher temporal resolution may allow for better identification of relevant intermediate states, based not only on the measured time-averaged KER but also on the time-resolved nuclear motion within a vibrational period and on quantum-beat structures in transiently populated electronic states [2–4,30]. This may eventually enable the *complete* identification of dissociation pathways in the XUV-triggered dissociation of small molecules. Moreover, the first encouraging attempts at FLASH have been undertaken to coincidently detect the emitted photoelectron(s) [34]. If successful, this will allow for the unambiguous energetic identification of the intermediate state involved within the achieved energy resolution.

In general, XUV pump pulses coherently populate more than one electronic state such that the vibrational wave function consists of a superposition of vibrational eigenstates in several electronic states. In future calculations [30], we plan to address the sensitivity of KER spectra on the coupling of adiabatic electronic states in the electric fields of the pump and probe pulses. Higher selectivity in the XUV population of electronic states can be achieved by analyzing the data as a function of the alignment of the molecules. The current data contain the full information on the molecular alignment, but due to limited statistics have not been analyzed to reveal this alignment dependence. In a future experiment with better statistics, we hope to be able to examine dissociation pathways for selected molecular alignment angles. An approach to increase the statistics even further without increasing the data acquisition times would be to employ nonadiabatic alignment [35] and

orientation in intense laser fields [36,37] in conjunction with XUV-pump–XUV-probe experiments.

ACKNOWLEDGMENTS

We acknowledge fruitful discussions with Lew Cocke and are greatly indebted to the scientific and technical team at FLASH, in particular, the machine operators and run coordinators, in striving for optimal beam-time conditions. Support from the Max-Planck Advanced Study Group at CFEL and the DFG via the Emmy-Noether and International Collaboration in Chemistry programs, and the Cluster of Excellence: Munich Center for Advanced Photonics is gratefully acknowledged. Y.H.J. is grateful for support from Shanghai Project No. 09310210Z1 and funding from the Chinese Academy of Sciences. The Kansas State University group was supported by the Chemical Sciences, Geosciences, and Biosciences Division, Office of Basic Energy Sciences, Office of Science, US Department of Energy. NGJ and IBI were also supported in part by the US National Science Foundation, Grant No. CHE-0822646. M.M. and U.T. were also supported in part by the U.S. National Science Foundation, Grant No. PHY 1068752.

[1] I. A. Bocharova, A. S. Alnaser, U. Thumm, T. Niederhausen, D. Ray, C. L. Cocke, and I. V. Litvinyuk, Phys. Rev. A **83**, 013417 (2011).

[2] S. De, M. Magrakvelidze, I. A. Bocharova, D. Ray, W. Cao, I. Znakovskaya, H. Li, Z. Wang, G. Laurent, U. Thumm, M. F. Kling, I. V. Litvinyuk, I. Ben-Itzhak, and C. L. Cocke, Phys. Rev. A **84**, 043410 (2011).

[3] B. Feuerstein, Th. Ergler, A. Rudenko, K. Zrost, C. D. Schröter, R. Moshammer, J. Ullrich, T. Niederhausen, and U. Thumm, Phys. Rev. Lett. **99**, 153002 (2007).

[4] U. Thumm, T. Niederhausen, and B. Feuerstein, Phys. Rev. A **77**, 063401 (2008).

[5] S. De, I. A. Bocharova, M. Magrakvelidze, D. Ray, W. Cao, B. Bergues, U. Thumm, M. F. Kling, I. V. Litvinyuk, and C. L. Cocke, Phys. Rev. A **82**, 013408 (2010).

[6] Th. Ergler, A. Rudenko, B. Feuerstein, K. Zrost, C. D. Schröter, R. Moshammer, and J. Ullrich, Phys. Rev. Lett. **95**, 093001 (2005).

[7] E. Goulielmakis, M. Schultze, M. Hofstetter, V. S. Yakovlev, J. Gagnon, M. Uiberacker, A. L. Aquila, E. M. Gullikson, D. T. Attwood, R. Kienberger, F. Krausz, and U. Kleineberg, Science **320**, 1614 (2008).

[8] A. L'Huillier, L. A. Lompre, G. Mainfray, and C. Manus, Phys. Rev. A **27**, 2503 (1983).

[9] F. Krausz and M. Ivanov, Rev. Mod. Phys. **81**, 163 (2009).

[10] M. Hoener, L. Fang, O. Kornilov, O. Gessner, S. T. Pratt, M. Gühr, E. P. Kanter, C. Blaga, C. Bostedt, J. D. Bozek, P. H. Bucksbaum, C. Buth, M. Chen, R. Coffee, J. Cryan, L. DiMauro, M. Glownia, E. Hosler, E. Kukk, S. R. Leone, B. McFarland, M. Messerschmidt, B. Murphy, V. Petrovic, D. Rolles, and N. Berrah, Phys. Rev. Lett. **104**, 253002 (2010).

[11] W. Cao, S. De, K. P. Singh, S. Chen, M. S. Schöffler, A. S. Alnaser, I. A. Bocharova, G. Laurent, D. Ray, S. Zherebtsov, M. F. Kling, I. Ben-Itzhak, I. V. Litvinyuk, A. Belkacem, T. Osipov, T. Rescigno, and C. L. Cocke, Phys. Rev. A **82**, 043410 (2010).

[12] W. Cao, G. Laurent, S. De, M. Schöffler, T. Jahnke, A. S. Alnaser, I. A. Bocharova, C. Stuck, D. Ray, M. F. Kling, I. Ben-Itzhak, Th. Weber, A. L. Landers, A. Belkacem, R. Dörner, A. E. Orel, T. N. Rescigno, and C. L. Cocke, Phys. Rev. A **84**, 053406 (2011).

[13] E. Gagnon, P. Ranitovic, X. M. Tong, C. L. Cocke, M. M. Murnane, H. C. Kapteyn, and A. S. Sandhu, Science **317**, 1374 (2007).

[14] F. Kelkensberg, C. Lefebvre, W. Siu, O. Ghafur, T. T. Nguyen-Dang, O. Atabek, A. Keller, V. Serov, P. Johnsson, M. Swoboda, T. Remetter, A. L'Huillier, S. Zherebtsov, G. Sansone, E. Benedetti, F. Ferrari, M. Nisoli, F. Lepine, M. F. Kling, and M. J. J. Vrakking, Phys. Rev. Lett. **103**, 123005 (2009).

[15] A. S. Sandhu, E. Gagnon, R. Santra, V. Sharma, W. Li, P. Ho, P. Ranitovic, C. L. Cocke, M. M. Murnane, and H. C. Kapteyn, Science **322**, 1081 (2008).

[16] G. Sansone, F. Kelkensberg, J. F. Perez-Torres, F. Morales, M. F. Kling, W. Siu, O. Ghafur, P. Johnsson, M. Swoboda, E. Benedetti, F. Ferrari, F. Lepine, J. L. Sanz-Vicario, S. Zherebtsov, I. Znakovskaya, A. L'Huillier, M.Yu. Ivanov, M. Nisoli, F. Martin, and M. J. J. Vrakking, Nature **465**, 763 (2010).

[17] A. Rudenko, Y. H. Jiang, M. Kurka, K. U. Kühnel, L. Foucar, O. Herrwerth, M. Lezius, M. F. Kling, C. D. Schröter, R. Moshammer, and J. Ullrich, J. Phys. B **43**, 194004 (2010).

[18] Y. H. Jiang, A. Rudenko, J. F. Perez-Torres, O. Herrwerth, L. Foucar, M. Kurka, K. U. Kühnel, M. Toppin, E. Plesiat, F. Morales, F. Martin, M. Lezius, M. F. Kling, T. Jahnke, R. Dörner, J. L. Sanz-Vicario, J. van Tilborg, A. Belkacem, M. Schulz, K. Ueda, T. J. M. Zouros, S. Düsterer, R. Treusch, C. D. Schröter, R. Moshammer, and J. Ullrich, Phys. Rev. A **81**, 051402(R) (2010).

[19] Y. H. Jiang, A. Rudenko, O. Herrwerth, L. Foucar, M. Kurka, K. U. Kühnel, M. Lezius, M. F. Kling, J. van Tilborg, A. Belkacem, K. Ueda, S. Düsterer, R. Treusch, C. D. Schröter, R. Moshammer, and J. Ullrich, Phys. Rev. Lett. **105**, 263002 (2010).

[20] J. Ullrich, R. Moshammer, A. Dorn, R. Dörner, L. P. H. Schmidt, and H. Schmidt-Böcking, Rep. Prog. Phys. **66**, 1463 (2003).

[21] Y. H. Jiang, A. Rudenko, M. Kurka, K. U. Kühnel, Th. Ergler, L. Foucar, M. Schöffler, S. Schössler, T. Havermeier, M. Smolarski, K. Cole, R. Dörner, S. Düsterer, R. Treusch, M. Gensch, C. D. Schröter, R. Moshammer, and J. Ullrich, Phys. Rev. Lett. **102**, 123002 (2009).

[22] Y. H. Jiang, T. Pfeifer, A. Rudenko, O. Herrwerth, L. Foucar, M. Kurka, K. U. Kühnel, M. Lezius, M. F. Kling, X. Liu, K. Ueda, S. Düsterer, R. Treusch, C. D. Schröter, R. Moshammer, and J. Ullrich, Phys. Rev. A **82**, 041403(R) (2010).

[23] B. Feuerstein and U. Thumm, Phys. Rev. A **67**, 063408 (2003).

[24] M. Lundqvist, D. Edvardsson, P. Baltzer, M. Larsson, and B. Wannberg, J. Phys. B **29**, 499 (1996).
[25] C. M. Marian, R. Marian, S. D. Peyerimhoff, B. A. Hess, R. J. Buenker, and G. Seger, Mol. Phys. **46**, 779 (1982).
[26] J. Steinfeld, *Molecules and Radiation* (Dover Publications, New York, 2005).
[27] S. Voss, A. S. Alnaser, X. M. Tong, C. Maharjan, P. Ranitovic, B. Ulrich, B. Shan, Z. Chang, C. D. Lin, and C. L. Cocke, J. Phys. B **37**, 4239 (2004).
[28] B. H. Brandsen and C. J. Joachain, *Physics of Atoms and Molecules* (Person Education Limited, Essex, England, 2003).
[29] L. Quaglia, O. Chiappa, G. Granucci, V. Brenner, Ph. Millie, and C. Cornaggia, J. Phys. B **35**, L145 (2002).
[30] M. Magrakvelidze, C. M. Aikens, and U. Thumm (to be published).
[31] T. Aoto, K. Ito, Y. Hikosaka, A. Shibasaki, R. Hirayama, N. Yamamono, and E. Miyoshi, J. Chem. Phys. **124**, 234306 (2006).
[32] M. Lundqvist, D. Edvardsson, P. Baltzer, and B. Wannberg, J. Phys. B **29**, 1489 (1996).
[33] P. Baltzer, M. Larsson, L. Karlsson, B. Wannberg, and M. Carlsson Gothe, Phys. Rev. A **46**, 5545 (1992).
[34] M. Kurka, A. Rudenko, L. Foucar, K. U. Kühnel, Y. H. Jiang, T. Ergler, T. Havermeier, M. Smolarski, S. Schössler, K. Cole, M. Schöffler, R. Dörner, M. Gensch, S. Düsterer, R. Treusch, S. Fritzsche, A. N. Grum-Grzhimailo, E. V. Gryzlova, N. M. Kabachnik, C. D. Schröter, R. Moshammer, and J. Ullrich, J. Phys. B **42**, 141002 (2009).
[35] F. Lépine, M. F. Kling, Y. Ni, J. Khan, O. Ghafur, T. Martchenko, E. Gustafsson, P. Johnsson, K. Varjú, T. Remetter, and A. L'Huillier, J. Mod. Opt. **54**, 953 (2007).
[36] S. De, I. Znakovskaya, D. Ray, F. Anis, Nora G. Johnson, I. A. Bocharova, M. Magrakvelidze, B. D. Esry, C. L. Cocke, I. V. Litvinyuk, and M. F. Kling, Phys. Rev. Lett. **103**, 153002 (2009).
[37] A. M. Sayler, P. Q. Wang, K. D. Carnes, B. D. Esry, and I. Ben-Itzhak, Phys. Rev. A **75**, 063420 (2007).